

Manifold-valued Image Generation with Wasserstein Adversarial Networks

Zhiwu Huang[†], Jiqing Wu[†], Luc Van Gool^{†‡}

[†]Computer Vision Lab, ETH Zurich, Switzerland [‡]VISICS, KU Leuven, Belgium

{zhiwu.huang, jiqing.wu, vangool}@vision.ee.ethz.ch

Abstract

Unsupervised image generation has recently received an increasing amount of attention thanks to the great success of generative adversarial networks (GANs), particularly Wasserstein GANs. Inspired by the paradigm of real-valued image generation, this paper makes the first attempt to formulate the problem of generating manifold-valued images, which are frequently encountered in real-world applications. For the study, we specially exploit three typical manifold-valued image generation tasks: hue-saturation-value (HSV) color image generation, chromaticity-brightness (CB) color image generation, and diffusion-tensor (DT) image generation. In order to produce such kinds of images as realistic as possible, we generalize the state-of-the-art technique of Wasserstein GANs to the manifold context with exploiting Riemannian geometry. For the proposed manifold-valued image generation problem, we recommend three benchmark datasets that are CIFAR-10 HSV/CB color images, ImageNet HSV/CB color images, UCL DT image datasets. On the three datasets, we experimentally demonstrate the proposed manifold-aware Wasserstein GAN can generate high quality manifold-valued images.

1. Introduction

Recent advances in real-valued image generation with neural networks have made it feasible to generate diverse natural images that capture the high-level structure of the training data. One of the most striking successes in unsupervised image generation have involved generative adversarial network (GAN) techniques [19, 31, 36, 11, 28], which estimate generative models via an adversarial process. The state-of-the-art GANs [1, 20] essentially try to learn the distribution of real data by minimizing Wasserstein distance in probability distribution by generating adversarial data.

In this paper, we come up with a new problem of manifold-valued image generation. Actually, images having values on a manifold are also of much interest in a variety of applications. For instance, images with each

pixel being on the circle \mathbb{S}^1 often appear in Interferometric Synthetic Aperture Radar (InSAR) for geodesy and remote sensing [13, 16]. Diffusion-tensor magnetic resonance imaging (DT-MRI) [35, 34, 32, 30] generally processes images with values on the manifold of symmetric positive definite 3×3 matrices SPD(3). In Electron Backscatter Diffraction (EBSD) analysis [4, 6], the treated images have pixels in the group of rotations SO(3) modulo the crystal's symmetry group. Furthermore, many manifold-valued image processing techniques [7, 5, 10, 3, 24] arise when working in phase-based color spaces that are more adapted to human color perception than the RGB space, such as hue-saturation-value (HSV) and chromaticity-brightness (CB). In the HSV and CB images, each pixel value reside on the product manifolds $\mathbb{S}^1 \times \mathbb{R}^2$ and $\mathbb{S}^2 \times \mathbb{R}^1$ respectively.

Processing manifold-valued images proposes new challenges in the new problem of image generation as well as classical image processing tasks like denoising, inpainting, and segmentation [7, 9, 5, 10, 3, 8, 24]. To better handle the problem, we generalize the generative model of Wasserstein GANs by exploiting Riemannian geometry of the involved manifolds. Without loss of generality, we take three typical types of manifold-valued images for study, and propose a manifold-aware Wasserstein GAN approach to produce plausible samples residing on such manifolds. In summary, the paper gives rise to two original contributions:

- To the best of our knowledge, this paper proposes the novel problem of unsupervised manifold-valued image generation for the first time in the existing literature.
- We generalize the Wasserstein GAN approach to the Riemannian manifold setting so as to address the problem of manifold-valued image generation.

2. Background

2.1. Real-valued Image Generation

Natural images are examples of what our visual world looks like and we refer to these as samples from the true data distribution \mathbb{P}_r . Typically, this kind of image values are Euclidean-valued (or real-valued). In other words, their

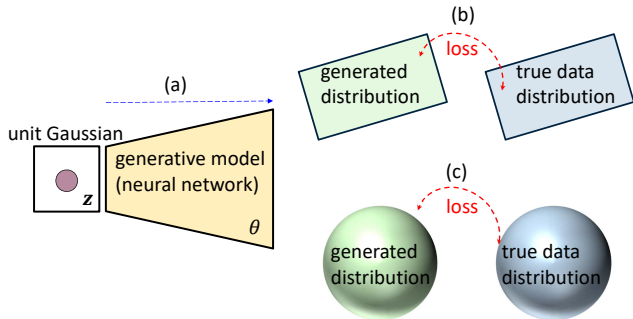


Figure 1. Conceptual illustration of real-valued image generation (a)→(b) where the data lie in flat Euclidean spaces, and manifold-valued image generation (a)→(c) where the data reside on non-flat Riemannian manifolds.

geometrical structure can be respected well with using classical Euclidean metric. Accordingly, the image generation problem is concerned with learning the true data probability distribution. The classical solution is to learn a probability density, which may not exist in practice. In contrast, there also exists another typical approach that directly generates samples following a certain distribution \mathbb{P}_g , which approximates the true data distribution. As studied in [1] the approach is useful in two ways. First of all, this approach is able to represent distributions confined to a low dimensional manifold, which is easier to estimate. Second, the capability to generate samples easily is often more useful than estimating the numerical value of the density.

Mathematically, one can consider a dataset of examples $\mathbf{x}_1, \dots, \mathbf{x}_n$ as samples from a real data distribution $\mathbb{P}_r(\mathbf{x})$. As shown in Fig. 1 (a)→(b), the blue region shows the part of the image space that, with a high probability consists of real images, and the elements in the space indicate the data points (each is one image). Now, the model also represents a distribution $\mathbb{P}_g(\mathbf{x})$ (green) that is defined implicitly by taking points from a unit Gaussian distribution (red) and mapping them through a neural network named the generative model (yellow). The network is a function with parameters θ , and learning these parameters will learn the generated distribution of images. The goal is then to seek parameters θ that produce a distribution that matches the real data distribution closely (for example, by having a small Wasserstein-1 distance). Therefore, one can imagine that the green distribution starting out random and then the training process iteratively updating the parameters θ to stretch and squeeze it to better match the blue distribution. The core of the generation process is how to make the distribution of generated data close to the true data distribution, that is how to define the distribution distance. One of the most important measurement is Wasserstein-1 or Earth-Mover distance

$$W(\mathbb{P}_r, \mathbb{P}_g) = \inf_{\gamma \in \Pi(\mathbb{P}_r, \mathbb{P}_g)} \mathbb{E}_{(\mathbf{x}, \mathbf{y}) \sim \gamma} [\|\mathbf{x} - \mathbf{y}\|], \quad (1)$$

where $\Pi(\mathbb{P}_r, \mathbb{P}_g)$ denotes the set of all joint distributions $\gamma(\mathbf{x}, \mathbf{y})$ whose marginals are $\mathbb{P}_r, \mathbb{P}_g$ respectively. Intuitively, $\gamma(\mathbf{x}, \mathbf{y})$ indicates how much mass should be transported from \mathbf{x} to \mathbf{y} in order to transform the distributions \mathbb{P}_r into the distribution \mathbb{P}_g . The Wasserstein distance then is the cost of the optimal transport plan.

2.2. Wasserstein GANs

For real-valued image generation, the state-of-the-art techniques are Generative Adversarial Networks (GANs) [19, 31, 36, 11, 28]. The GAN framework establishes a min-max adversarial game between two competing networks. The generator network G maps a source of noise to the input space. The discriminator network D receives either a generated sample or a true data sample and must distinguish between the two. The generator is trained to fool the discriminator. Theoretically, the original GAN framework actually minimizes Jensen-Shannon divergence between the true data distribution and generated sample distribution.

By contrast, Wasserstein GAN [1] provided extensive theoretical work and showed empirically that alternatively minimizing a reasonable and efficient approximation of the Wasserstein-1 distance is a theoretically sound optimization problem. For this approximation of the Wasserstein-1 distance to be valid, the original Wasserstein GAN imposed weight clipping constraints on the critic (referred to as the discriminator pre-Wasserstein) such that the optimal map of the discriminator is Lipschitz continuous. However, as proved in [20], the set of functions satisfying this constraint is merely a subset of the k -Lipschitz functions for some k which depends on the clipping threshold and the critic architecture, which inevitably causes some training failures. To address this issue, improved training of Wasserstein GAN [20] enables very stable GAN training by penalizing the norm of the gradient of the critic with respect to its inputs instead of clipping weights. In particular, this gradient penalty is simply added to the basic Wasserstein GAN loss for the following full objective:

$$\min_G \max_D \mathbb{E}_{\mathbf{x} \sim \mathbb{P}_r} [D(\mathbf{x})] - \mathbb{E}_{G(\mathbf{z}) \sim \mathbb{P}_g} [D(G(\mathbf{z}))] + \lambda \mathbb{E}_{\hat{\mathbf{x}} \sim \mathbb{P}_{\hat{\mathbf{x}}}} [(\|\nabla_{\hat{\mathbf{x}}} D(\hat{\mathbf{x}})\|_2 - 1)^2], \quad (2)$$

where \mathbf{z} is random noise, $\hat{\mathbf{x}}$ is random samples following the distribution $\mathbb{P}_{\hat{\mathbf{x}}}$ that is sampled uniformly along straight lines between pairs of points sampled from \mathbb{P}_r and \mathbb{P}_g , $\nabla_{\hat{\mathbf{x}}} D(\hat{\mathbf{x}})$ is the gradient w.r.t $\hat{\mathbf{x}}$, $G(\cdot)$, $D(\cdot)$ denotes the functions of generator and discriminator respectively.

3. Manifold-valued Image Generation

3.1. Manifold-valued Images

In this paper, we concentrate on three typical types of manifold-valued images.

HSV Images: Each pixel in the HSV color model can be represented by a triple which specifies hue, saturation and value respectively. As hue value is phase-based, the HSV data actually live on the product manifold of a Cyclic manifold and vector spaces $\mathcal{H} = \mathbb{S}^1 \times [0, 1]^2$.

CB Images: Each pixel in the CB color model contains chromaticity and brightness components. Since our focus is on manifold-valued data, the whole paper studies the chromaticity (spherical) component lying on \mathbb{S}^2 for CB images.

DT Images: In diffusion tensor (DT) images, each voxel is represented with a 3×3 tensor, that is symmetric positive definite (SPD) matrix. It is known that the data of DT images reside on the manifold SPD(3) of SPD matrices.

3.2. Problem Formulation

In analogy to real-valued image generation, the task of manifold-valued image generation is to generate samples respecting a certain distribution for learning the distribution of real manifold-valued data. As shown in Fig.1 (a)→(c), the manifold-valued data live on non-flat Riemannian manifolds rather than a flat Euclidean space. In the manifold setting, applying traditional generative models directly to the non-Euclidean data would seriously affect the generation. Accordingly, by comparing with real-valued image generation, manifold-valued image generation proposes two of the most important issues that are: 1) the definition on the distribution of manifold-valued data, and 2) the generalization of the distribution (Wasserstein) distance to manifolds.

To address the first issue, there exist some works like [30, 2, 22, 21]. On a Riemannian manifold, it is able to define probability density functions thanks to the availability of a tailored metric. In other words, all definitions of distribution can be derived from the Riemannian metric of the resulting manifold. Formally, let \mathbf{x}, \mathbf{y} be two points of the manifold that we consider as a local reference and \mathbf{v} a vector of the tangent space $T_{\mathbf{y}}\mathcal{M}$ at the point \mathbf{y} . The smoothly varying family of inner products in each tangent space is known as the Riemannian metric. From the theory of second-order differential equations, there has one and only one geodesic starting from that point with the tangent vector. This allows to span the curved manifold in the flat tangent space along the geodesics (think of rolling a sphere along its tangent plane at a given point). The geodesics going through the reference point \mathbf{y} are transformed into straight lines and the distance along these geodesics is preserved (at least in a neighborhood of \mathbf{y}). The function that maps to each tangent vector $\mathbf{v} \in T_{\mathbf{y}}\mathcal{M}$ the point \mathbf{x} of the manifold that is achieved by the geodesic starting at \mathbf{y} with this tangent vector is named the exponential map. This map is defined in the whole tangent space $T_{\mathbf{y}}\mathcal{M}$ (since the manifold is complete) but it is generally one-to-one only locally around $\mathbf{0}$ in the tangent space (i.e., around the reference point \mathbf{y} in the manifold). For mapping the manifold data

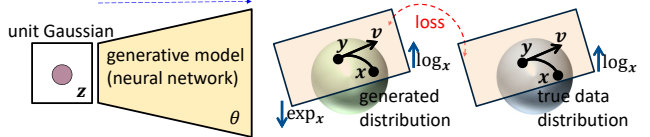


Figure 2. Overview of the proposed manifold-aware Wasserstein GAN (manifoldWGAN) approach for manifold-valued image generation. The manifoldWGAN introduces logarithm map and exponential map between Riemannian manifold and tangent space to the setting of Wasserstein GANs.

to the tangent space that respects Euclidean geometry, we denote $\mathbf{v} = \log_{\mathbf{y}}(\mathbf{x})$ as the inverse of the exponential map: this is the smallest vector such that $\mathbf{x} = \exp_{\mathbf{y}} \mathbf{v}$.

For the second issue, we suggest to generalize the Wasserstein-1 distance to Riemannian manifolds. As studied in [17, 33, 26], for optimal mass transport on real-valued data, the optimal map has a convex potential (i.e. $D(\mathbf{x}) = \nabla \phi(\mathbf{x})$ with $\phi(\mathbf{x})$ being convex) and is shown to be the only map with convex potential. From the studies of [27, 15, 18], for the manifold case, the optimal map can be expressed as a so-called gradient map:

Theorem 1. *Let \mathcal{M} be a smooth compact Riemannian manifold, and consider the cost $c = d^2/2$, with d being the Riemannian distance metric. Given two probability distributions \mathbb{P}_r and \mathbb{P}_g supported on the manifold \mathcal{M} , there exists a convex potential function $\phi : \mathcal{M} \rightarrow \mathbb{R} \cup \{+\infty\}$ such that $D(\mathbf{x}) = \exp_{\mathbf{y}}(\nabla_g \phi(\mathbf{x}))$ is the unique optimal transport map sending \mathbb{P}_r to \mathbb{P}_g , where ∇_g indicates the gradient with respect to the Riemannian metric $g = \langle \log_{\mathbf{y}}(\mathbf{x}_1), \log_{\mathbf{y}}(\mathbf{x}_2) \rangle$ on the manifold \mathcal{M} .*

Inspired by the original Wasserstein distance Eqn.1 in a Euclidean setting, we present the new Wasserstein distance on the underlying Riemannian manifold with leveraging its logarithm map that yields Euclidean representations:

$$W(\mathbb{P}_r, \mathbb{P}_g) = \inf_{\gamma \in \Pi(\mathbb{P}_r, \mathbb{P}_g)} \mathbb{E}_{(\mathbf{x}, \mathbf{y}) \sim \gamma} [\|\log_{\mathbf{y}}(\mathbf{x}) - \log_{\mathbf{y}}(\mathbf{y})\|], \quad (3)$$

where \mathbf{x}, \mathbf{y} are points on the manifold, $\Pi(\mathbb{P}_r, \mathbb{P}_g)$ indicates the set of all joint distributions $\gamma(\mathbf{x}, \mathbf{y})$, and $\gamma(\mathbf{x}, \mathbf{y})$ denotes how much mass will be transported from \mathbf{x} to \mathbf{y} .

4. Manifold-aware Wasserstein GAN

According to **Theorem 1** and the derived Wasserstein distance Eqn.3, we generalize the objective function Eqn.2 of Wasserstein GAN to Riemannian manifolds

$$\begin{aligned} \min_G \max_D \mathbb{E}_{\mathbf{x} \sim \mathbb{P}_r} [D(\log_{\mathbf{y}}(\mathbf{x}))] \\ - \mathbb{E}_{G(\mathbf{z}) \sim \mathbb{P}_g} [D(\log_{\mathbf{y}}(\exp_{\mathbf{y}}(G(\mathbf{z}))))] \quad (4) \\ + \lambda \mathbb{E}_{\hat{\mathbf{x}} \sim \mathbb{P}_{\hat{\mathbf{x}}}} [(\|\nabla_{\hat{\mathbf{x}}} D(\hat{\mathbf{x}})\|_2 - 1)^2], \end{aligned}$$

where $\log_{\mathbf{y}}(\cdot)$ and $\exp_{\mathbf{y}}(\cdot)$ are the logarithm and exponential maps respectively for the underlying manifold. As the logarithm map $\log_{\mathbf{y}}(\cdot)$ can project the manifold-valued data to Euclidean space, any regular networks can be applied directly to the resulting data. To generate valid manifold-valued data with using the generative network G , we employ exponential map $\exp_{\mathbf{y}}(\cdot)$ to transform the data back to the manifold. An overview of the proposed manifold-aware Wasserstein GAN (manifoldWGAN) approach is shown in Fig.2. As done in [20], $\mathbb{P}_{\hat{\mathbf{x}}}$ is also defined sampling uniformly along straight lines between pairs of points sampled from the data distribution \mathbb{P}_r and the generator distribution \mathbb{P}_g . In the context of manifold-valued data, we apply logarithm and exponential maps to the linear sampling:

$$\hat{\mathbf{x}} = (1 - t) \log_{\mathbf{y}}(\mathbf{x}) + t \log_{\mathbf{y}}(\exp_{\mathbf{y}}(G(\mathbf{z}))), \quad (5)$$

where $0 \leq t \leq 1$.

In this paper, our focus is on the generation of HSV, CB and DT images. Therefore, we consider the data on the product manifold $\mathcal{H} = \mathbb{S}^1 \times [0, 1]^2$, the spherical data on \mathbb{S}^n and the SPD data on $\text{SPD}(n)$. In the sequel, we specially study the forms for their resulting exponential map and logarithm map to achieve the objective Eqn.4.

Theorem 2. *As presented in [10], the geodesic distance of two points \mathbf{x}, \mathbf{y} on the product manifold $\mathcal{H} = \mathbb{S}^1 \times \mathbb{R}^2$ of combined cyclic and real-valued data:*

$$d(\mathbf{x}, \mathbf{y}) = \sqrt{\arccos(\mathbf{x}_{\mathbb{S}} \mathbf{y}_{\mathbb{S}}) + \|\mathbf{x}_{\mathbb{R}} - \mathbf{y}_{\mathbb{R}}\|^2}. \quad (6)$$

The logarithm and exponential maps associated with the distance metric are defined as

$$\begin{aligned} \log_{\mathbf{y}}(\mathbf{x}) &= [\text{mod}(\mathbf{x}_{\mathbb{S}} - \mathbf{y}_{\mathbb{S}}, 2\pi), \mathbf{x}_{\mathbb{R}} - \mathbf{y}_{\mathbb{R}}], \\ \exp_{\mathbf{y}}(\mathbf{v}) &= [\text{mod}(\mathbf{v}_{\mathbb{S}} + \mathbf{y}_{\mathbb{S}}, 2\pi), \mathbf{v}_{\mathbb{R}} + \mathbf{y}_{\mathbb{R}}], \end{aligned} \quad (7)$$

where *mod* denotes the modulo operation.

Theorem 3. [12, 25] presented the geodesic distance of two points \mathbf{x}, \mathbf{y} on the sphere manifold \mathbb{S}^n :

$$d(\mathbf{x}, \mathbf{y}) = \arccos(\text{trace}(\mathbf{x}^T \mathbf{y})). \quad (8)$$

The logarithm and exponential maps associated with the metric can be expressed:

$$\begin{aligned} \log_{\mathbf{y}}(\mathbf{x}) &= \frac{d(\mathbf{x}, \mathbf{y})}{\|p_{\mathbf{y}}(\mathbf{x} - \mathbf{y})\|_F} p_{\mathbf{y}}(\mathbf{x} - \mathbf{y}), \\ \exp_{\mathbf{y}}(\mathbf{v}) &= \cos(\|\mathbf{v}\|_F) \mathbf{y} + \frac{\sin(\|\mathbf{v}\|_F)}{\|\mathbf{v}\|_F} \mathbf{v}, \end{aligned} \quad (9)$$

where $\|\cdot\|_F$ indicates the Frobenius norm operation, $p_{\mathbf{y}}(\mathbf{H}) = \mathbf{H} - \text{trace}(\mathbf{y}^T \mathbf{H}) \mathbf{y}$.

Theorem 4. As studied in [2, 22], the Log-Euclidean Metric

$$d(\mathbf{x}, \mathbf{y}) = \|\log(\mathbf{x}) - \log(\mathbf{y})\|_F^2. \quad (10)$$

Algorithm 1 Manifold-aware Wasserstein GAN (manifoldWGAN), our proposed algorithm. All the experiments in the paper used the default values $\lambda = 10$, $n_{\text{critic}} = 5$.

Require: α , learning rate. m , the batch size. n_{critic} , the critic iterations per generation iteration. λ , the balance parameter of gradient norm penalty, \mathbf{w}_0 , initial critic parameters. θ_0 , initial generator's parameter.

```

1: while  $\theta$  has not converged do
2:   for  $t=0, \dots, n_{\text{critic}}$  do
3:     Sample  $\{\mathbf{x}^{(i)}\}_{i=1}^m \sim \mathbb{P}_r$  a batch from the real data.
4:     Sample  $\{\mathbf{z}^{(i)}\}_{i=1}^m \sim \mathbb{P}_g$  a batch of prior samples.
5:      $D_w \leftarrow \nabla_w [\mathcal{L}]$  where  $\mathcal{L}$  is computed by Eqn.4.
6:      $\mathbf{w} \leftarrow \mathbf{w} + \alpha \cdot \text{AdamOptimizer}(\mathbf{w}, D_w)$ 
7:   end for
8:   Sample  $\{\mathbf{z}^{(i)}\}_{i=1}^m \sim \mathbb{P}_g$  a batch of prior samples.
9:    $G_{\theta} \leftarrow \nabla_{\theta} [-\frac{1}{m} \sum_{i=1}^m D_w(\log_{\mathbf{y}}(\exp_{\mathbf{y}}(G_{\theta}(\mathbf{z}^{(i)}))))]$ 
10:   $\theta \leftarrow \theta + \alpha \cdot \text{AdamOptimizer}(\theta, G_{\theta})$ 
11: end while

```

for the SPD manifold $\text{SPD}(n)$ is derived by employing the Lie group structure under the group operation $\mathbf{x} \odot \mathbf{y} := \exp(\log(\mathbf{x}) + \log(\mathbf{y}))$ for $\mathbf{x}, \mathbf{y} \in \text{SPD}(n)$ where $\exp(\cdot)$ and $\log(\cdot)$ indicate the regular matrix exponential and logarithm operators. The logarithmic and exponential maps associated with the Log-Euclidean metric is expressed with matrix logarithms and exponential operations:

$$\begin{aligned} \log_{\mathbf{y}}(\mathbf{x}) &= D_{\log(\mathbf{y})} \exp.(\log(\mathbf{y}) - \log(\mathbf{x})), \\ \exp_{\mathbf{y}}(\mathbf{v}) &= \exp(\log(\mathbf{y}) + D_{\mathbf{y}} \log. \mathbf{v}), \end{aligned} \quad (11)$$

where $D_{\log(\mathbf{y})} \exp. = (D_{\mathbf{y}} \log.)^{-1}$ is achieved by the differentiation of the equality $\log \circ \exp = \mathbf{I}$, and here \mathbf{I} is the identity matrix.

Following such basic logarithm and exponential maps on the corresponding manifolds of the processed manifold-valued samples, the algorithm of the proposed manifoldWGAN is presented in Algorithm.1.

5. Experiment

In order to study the problem of manifold-valued image generation, we suggest three benchmark evaluations that use the HSV and CB images of the well-known CIFAR-10 [23], ImageNet [29], and the popular UCL DT image dataset [14]. In all the evaluations, we compare our proposed manifold-aware Wasserstein GAN (manifoldWGAN) against the state-of-the-art image generation technique Wasserstein GAN (WGAN)¹ [20] that has proved to improve the original WGAN [1].

In all the evaluations, we follow [20] to use residual network for both the generator and critic. The setting of the

¹We use the original authors' source code, which is available at https://github.com/igul222/improved_wgan_training

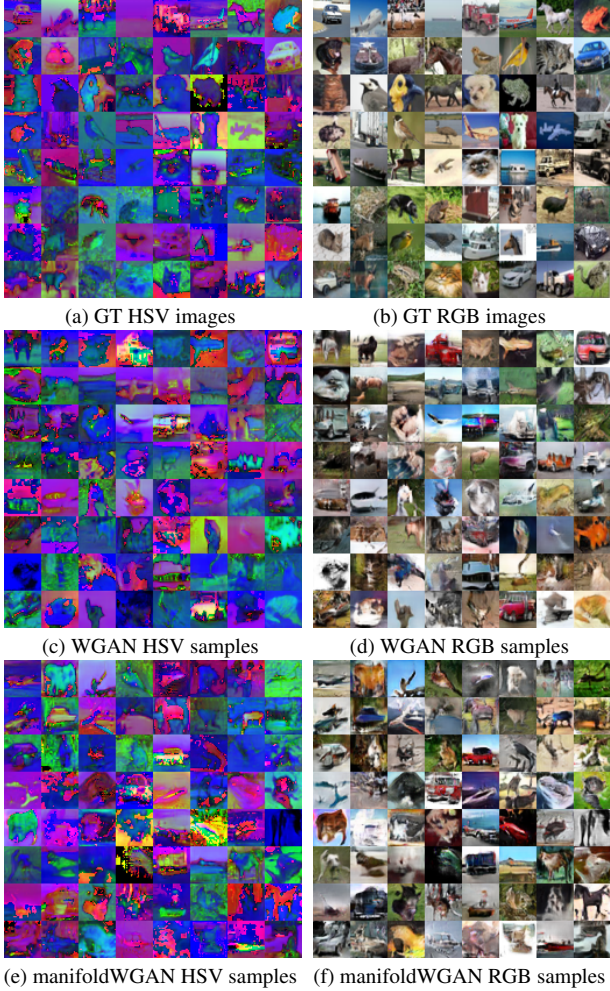


Figure 3. Generated samples of WGAN [20] and the proposed manifoldWGAN for HSV image generation on CIFAR-10 with ground truth (GT) images and translated RGB images.

employed residual networks is the same as the ones used in [20]. Specially, we utilize pre-activation residual blocks with two 3×3 convolutional layers and ReLU nonlinearity. Some residual blocks perform downsampling (in the critic) using mean pooling after the second convolutional layer, or nearest-neighbor upsampling (in the generator) before the second convolution. We employ batch normalization in the generator but not the critic. We finally optimize the network using Adam with learning rate 2×10^{-4} , decayed linearly to 0 over 100K generator iterations, and batch size 64. For further architectural details, please refer to the public implementation of [20]. For all the networks, we train each of them on a single GeForce GTX TITAN X GPU.

5.1. HSV Image Generation

For HSV color image generation, we choose the CIFAR-10 and ImageNet datasets, both of which are standard

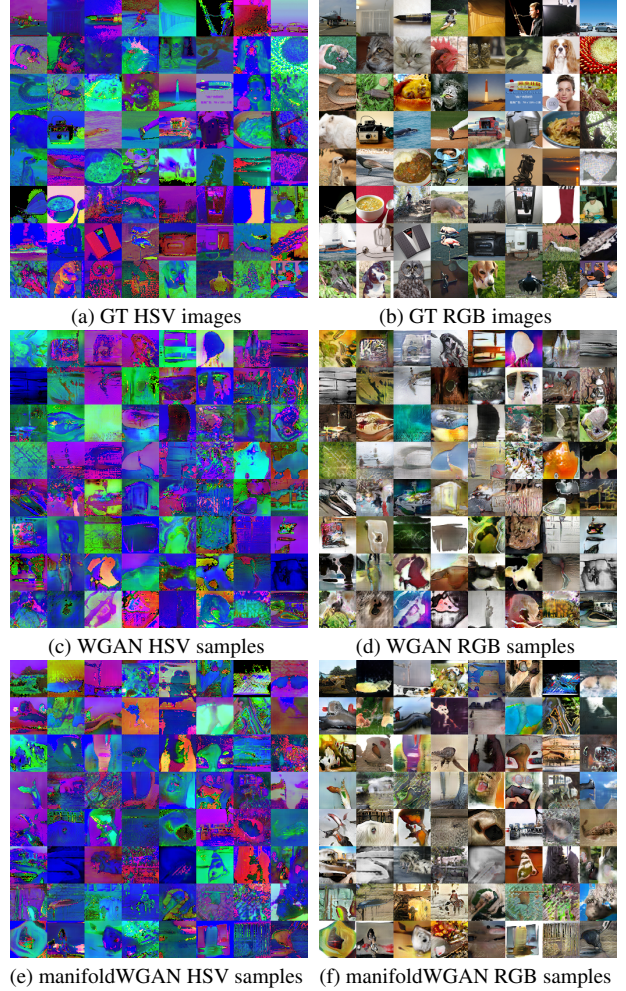


Figure 4. Generated samples of WGAN [20] and the proposed manifoldWGAN for HSV image generation on ImageNet with ground truth (GT) images and translated RGB images.

benchmarks in real-valued image generation. The CIFAR-10 dataset consists of 60000 32×32 colour images in 10 classes, with 6000 images per class. We use the 64×64 version of ImageNet, which contains 1,281,149 training images and 49,999 images for testing. To gather HSV color images whose values are on $\mathcal{H} = \mathbb{S}^1 \times [0, 1]^2$, we transfer the images from the RGB space to the HSV space.

For generating valid elements on $\mathcal{H} = \mathbb{S}^1 \times [0, 1]^2$, the proposed manifoldWGAN suggests to use the corresponding logarithm and exponential maps Eqn.7 (where each pixel value of the reference point \mathbf{y} is set to $[\pi, 0, 0]$) during the optimization of the objective Eqn.4, while the state-of-the-art generation technique WGAN treats the data as real-valued data with its original Wasserstein-based GAN loss.

Fig.3 and Fig.4 qualitatively show the generation results of WGAN and the proposed manifoldWGAN on CIFAR-10 and ImageNet respectively. The results justify that our

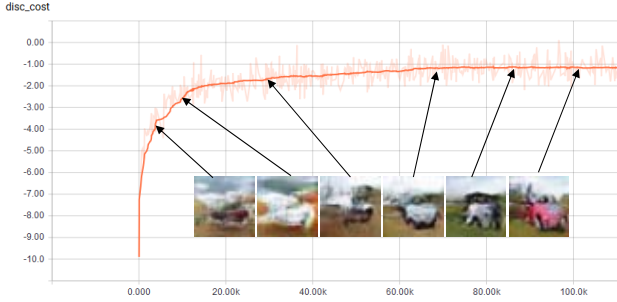


Figure 5. Training curves and generated samples (here, we show translated RGB samples) at different stages of training of the proposed manifoldWGAN on CIFAR-10 HSV image set. The value on y-axis denotes the negative critic cost (Wasserstein distance), and the value on the x-axis indicates the iteration number.

Method	Inception Score
DCGAN-RGB [31]	6.16
LSGAN-RGB [28]	6.47
WGAN-RGB [20]	7.86
WGAN-HSV [20]	6.01
manifoldWGAN-HSV	6.49

Table 1. Inception scores of different methods performing generation on RGB images or HSV images of the CIFAR-10 database

manifoldWGAN can generate more visually desirable HSV images, whose resulting RGB images appear to be somewhat better in both terms of image quality and semantic.

In addition, we also qualitatively compare WGAN and our manifoldWGAN on CIFAR-10 with respect to inception score. Note that we transfer the generated HSV images to RGB images for the inception score computation. Besides, we also enumerate results of the state-of-the-art generative models [31, 28, 20] performing on RGB images. The results reported in Table.1 demonstrate our manifoldWGAN performs better than WGAN for HSV image generation.

We finally show the training curves of negative Wasserstein GAN loss (Wasserstein distance) and generated samples at different stages of training in Fig.5. As we can see, the loss decreases consistently as training progresses and sample quality increases. This verifies a strong correlation between lower loss and better sample quality.

5.2. CB Image Generation

To evaluate our manifoldWGAN for image generation on the sphere manifold \mathbb{S}^2 , we collect CB images from CIFAR-10 and ImageNet. The setting on these two datasets are the same with above. In particular, we extract the chromaticity component of the CB images so that the generation problem on pure spherical data can be better studied.

As done in the last evaluation, we compare our manifold-



Figure 6. Generated samples of WGAN [20] and the proposed manifoldWGAN for CB image generation on CIFAR-10 (a1)-(b1)-(c1) and ImageNet (a2)-(b2)-(c2) with ground truths (GT)

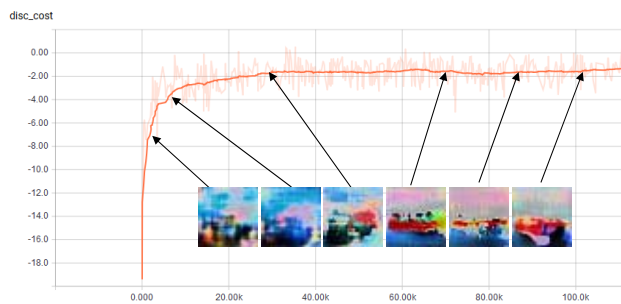


Figure 7. Training curves and generated samples at different stages of training of the proposed manifoldWGAN on CIFAR-10 CB image set. The values on y-axis and x-axis denote the negative critic cost (Wasserstein distance) and the iteration number respectively.

WGAN against the state-of-the-art GAN technique WGAN. Our manifoldWGAN proposes to make use of the mani-

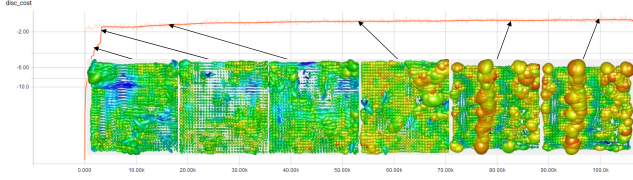


Figure 8. Training curves and generated samples at different stages of training of the proposed manifoldWGAN on UCL DT image set. The values on y-axis and x-axis denote the negative critic cost (Wasserstein distance) and the iteration number respectively.

fold geometry-aware logarithm and exponential maps Eqn.9 (where each pixel value of the anchor point \mathbf{y} is set to $[\frac{1}{\sqrt{3}}, \frac{1}{\sqrt{3}}, \frac{1}{\sqrt{3}}]$) on the sphere manifold during the sample generation. As shown in Fig.6, we discover that the WGAN approach generates samples with low-chromaticity, while the proposed manifoldWGAN can generate higher-quality samples. This shows the clear advantage of our method.

We also show the correlation between the proposed manifold-aware Wasserstein GAN loss and the quality of generated CB images in Fig.7. From the result, we can observe that the quality of generated CB samples tend to be better as the iteration number increases.

5.3. DT image Generation

We employ Camino brain DT image set [14] to evaluate our proposed manifoldWGAN for the SPD-valued image generation on SPD(3). The Camino project [14] provides a dataset of a Diffusion Tensor Magnetic Resonance Image (DT-MRI) of human heads, which is freely available² at <http://cmic.cs.ucl.ac.uk/camino>. The UCL DT image database contains 50 brain DT images in total. For data augmentation, we extract 26,080 DT slices of size 32×32 from the original DT images. Some ground truth DT slice images are listed in Fig.9 (a). Among the sampled DT slice images, there are around 0.6% non-SPD voxels in each DT slice on average, and only 2,399 samples contain no non-SPD voxels.

For generating visually favorable DT images, our manifoldWGAN suggests to introduce logarithm map and exponential map Eqn.11 (where each pixel value of the reference point \mathbf{y} is set to the identity matrix of size 3×3) on SPD manifolds to the Wasserstein GAN setting. In contrast, the original WGAN treats the SPD data as real-valued data. In order to make the generated samples of WGAN become valid DT (SPD-valued) images, we additionally employ our presented exponential map to transform the outputs of WGAN to the data on SPD manifolds. In Fig.9, we quantitatively compare these two different approaches on the UCL DT image set. Note that, to plot the gener-

ated DT images, we leverage the Manifold-valued Image Restoration Toolbox³. From the results, we can discover that the generated samples of WGAN is not plausible at all, while our manifoldWGAN can often synthesize highly realistic DT samples. Besides, it is also worth pointing out our model sometimes produces some noisy data owing to the noisy training data, which was pointed out above.

As the last two evaluations, we also study the relationship between the proposed manifold-aware Wasserstein loss and the generated sample quality in Fig.8. As the network training iterations increases, the negative Wasserstein loss goes up quickly and the visual quality of the generated DT images is also improved, again showing there are clear correlations among our manifoldWGAN loss, the convergence property and the quality of its generated samples.

6. Discussion and Outlook

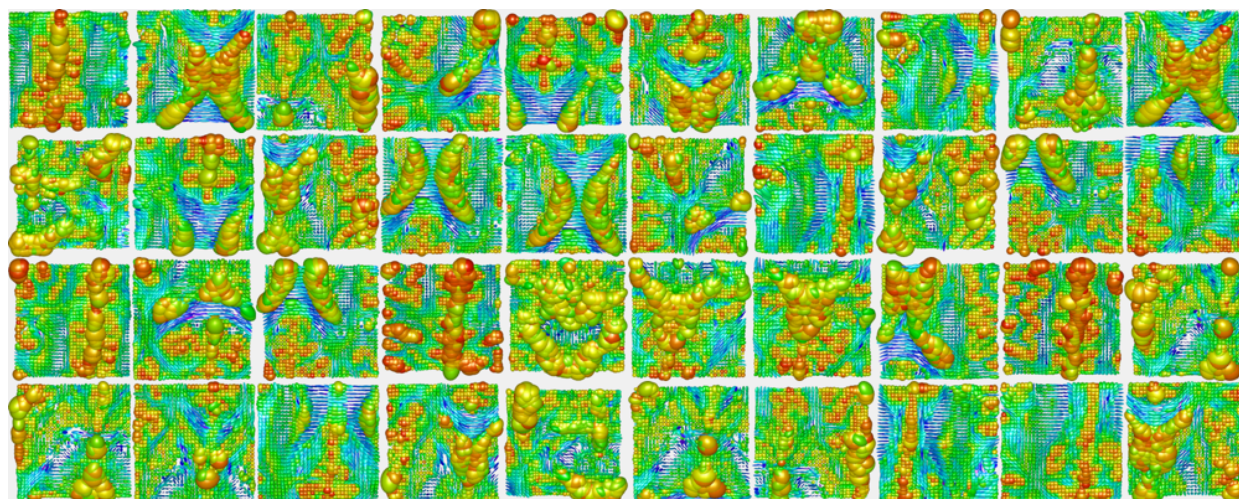
In this work we introduced a new problem of manifold-valued image generation, which can be applied to a wide variety of applications including InSAR, DT-MRI, EBSD and HSV/CB color imaging. In contrast to the real-valued image generation problem, generation on manifold-valued images is to produce samples that reside on non-flat Riemannian manifold.

As studied in the paper, it is non-trivial to apply the existing image generation technique directly to the context of manifold-valued image generation. To address the issue, we generalize the state-of-the-art Wasserstein GAN technique to manifold-valued generation with introducing a manifold geometry-aware learning framework. As classic manifold-based learning method, our approach equips the Wasserstein GAN framework with the basic logarithm map and exponential map that encourages computing the Wasserstein distance of the manifold-valued data. Without loss of generality, we applied the presented approach to the generation task on HSV, CB and DT images which reside on product manifold, sphere manifold and SPD manifold respectively. We finally suggested three standard benchmarks to evaluate our method on the three types of manifold-valued image generation tasks, and clearly show the superiority of our approach over the state-of-the-art WGAN.

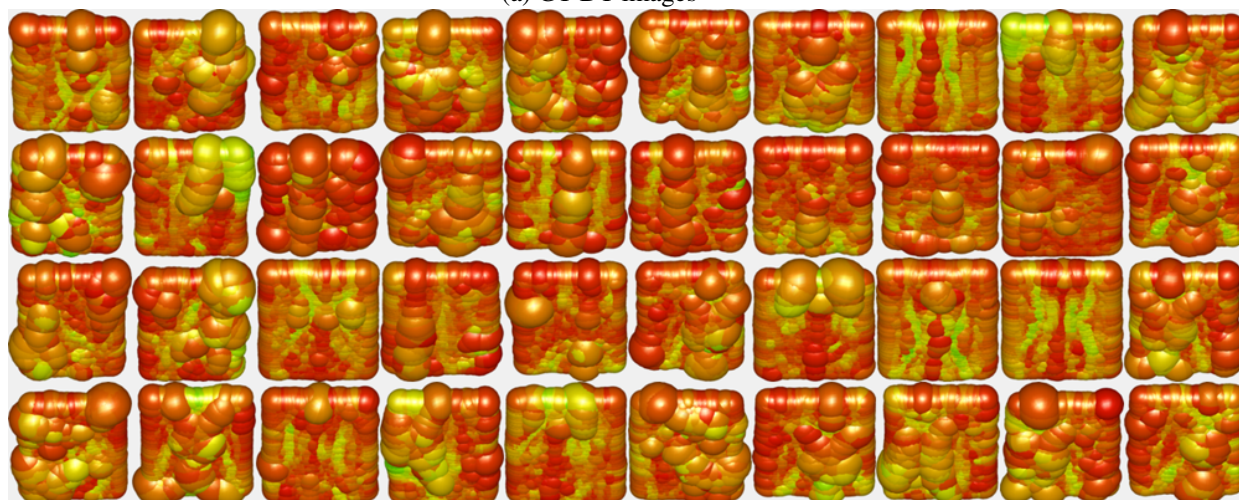
The proposed framework admits many straightforward extensions. First of all, we hope our work opens the path for more manifold-valued image generation tasks like shape manifold-valued data generation. Like real-valued image generation, we also encourage more works to extend our framework to conditional settings and even semi-supervised learning. Last but not least, the direction of exploiting adversarial manifold-valued samples would be very useful to a broad number of classical manifold-valued image processing tasks like denoising, inpainting and segmentation.

²To obtain the data, one can follow the tutorial at <http://cmic.cs.ucl.ac.uk/camino//index.php?n=Tutorials.DTI>

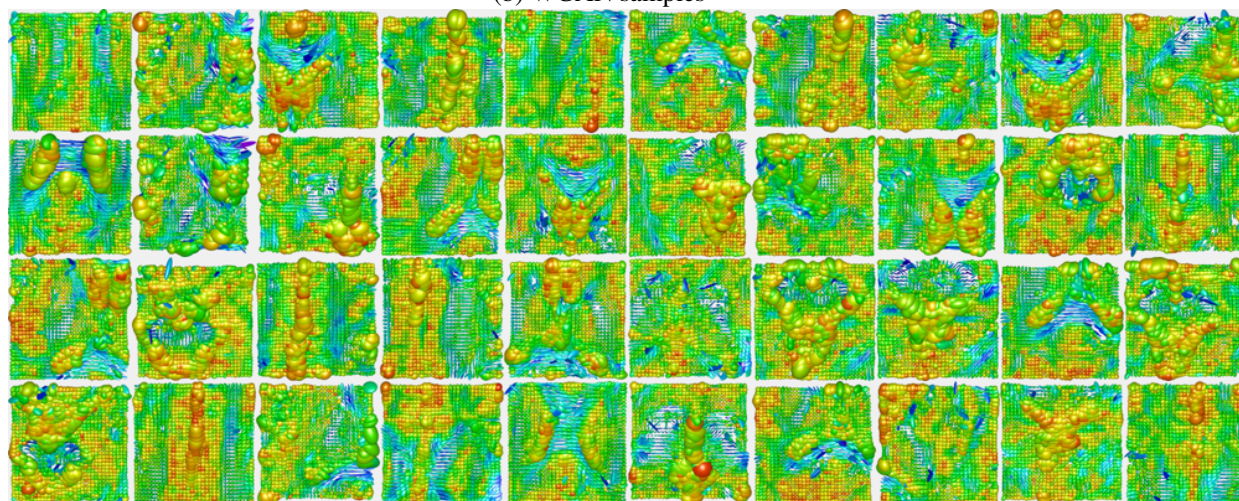
³The toolbox is available at <http://www.mathematik.uni-kl.de/imagepro/members/bergmann/mvirt/>.



(a) GT DT images



(b) WGAN samples



(c) manifoldWGAN samples

Figure 9. Generated samples of WGAN [20] and the proposed manifoldWGAN for DT image generation on the UCL DT image dataset with ground truth (GT) images. The figure is better viewed via zooming in.

Acknowledgements

We would like to thank Dr. Ronny Bergmann for his help on diffusion MRI processing, NVidia for donating the GPUs employed in this work.

References

- [1] M. Arjovsky, S. Chintala, and L. Bottou. Wasserstein generative adversarial networks. In *ICML*, 2017. 1, 2, 4
- [2] V. Arsigny, P. Fillard, X. Pennec, and N. Ayache. Log-Euclidean metrics for fast and simple calculus on diffusion tensors. *Magnetic resonance in medicine*, 56(2):411–421, 2006. 3, 4
- [3] M. Bacák, R. Bergmann, G. Steidl, and A. Weinmann. A second order nonsmooth variational model for restoring manifold-valued images. *SIAM Journal on Scientific Computing*, 38(1):A567–A597, 2016. 1
- [4] F. Bachmann, R. Hielscher, and H. Schaeben. Grain detection from 2d and 3d ebsd dataspecification of the mtex algorithm. *Ultramicroscopy*, 111(12):1720–1733, 2011. 1
- [5] S. Bansal and A. Tatu. Active contour models for manifold valued image segmentation. *Journal of Mathematical Imaging and Vision*, 52(2):303–314, 2015. 1
- [6] R. Bergmann, R. H. Chan, R. Hielscher, J. Persch, and G. Steidl. Restoration of manifold-valued images by half-quadratic minimization. *arXiv preprint arXiv:1505.07029*, 2015. 1
- [7] R. Bergmann, F. Laus, G. Steidl, and A. Weinmann. Second order differences of cyclic data and applications in variational denoising. *SIAM Journal on Imaging Sciences*, 7(4):2916–2953, 2014. 1
- [8] R. Bergmann and D. Tenbrinck. Nonlocal inpainting of manifold-valued data on finite weighted graphs. *arXiv preprint arXiv:1704.06424*, 2017. 1
- [9] R. Bergmann and A. Weinmann. Inpainting of cyclic data using first and second order differences. *EMM-CVPR, Lecture Notes in Computer Science*, pages 155–168, 2015. 1
- [10] R. Bergmann and A. Weinmann. A second-order TV-type approach for inpainting and denoising higher dimensional combined cyclic and vector space data. *Journal of Mathematical Imaging and Vision*, 55(3):401–427, 2016. 1, 4
- [11] D. Berthelot, T. Schumm, and L. Metz. BEGAN: Boundary equilibrium generative adversarial networks. *arXiv preprint arXiv:1703.10717*, 2017. 1, 2
- [12] R. Bhattacharya and V. Patrangenu. Nonparametric estimation of location and dispersion on Riemannian manifolds. *Journal of Statistical Planning and Inference*, 108(1):23–35, 2002. 4
- [13] R. Bürgmann, P. A. Rosen, and E. J. Fielding. Synthetic aperture radar interferometry to measure earths surface topography and its deformation. *Annual review of earth and planetary sciences*, 28(1):169–209, 2000. 1
- [14] P. Cook, Y. Bai, S. Nedjati-Gilani, K. Seunarine, M. Hall, G. Parker, and D. Alexander. Camino: open-source diffusion-mri reconstruction and processing. In *14th scientific meeting of the international society for magnetic resonance in medicine*, volume 2759. Seattle WA, USA, 2006. 4, 7
- [15] G. De Philippis and A. Figalli. The monge-ampère equation and its link to optimal transportation. *Bulletin of the American Mathematical Society*, 51(4):527–580, 2014. 3
- [16] C.-A. Deledalle, L. Denis, and F. Tupin. NI-insar: Nonlocal interferogram estimation. *IEEE Transactions on Geoscience and Remote Sensing*, 49(4):1441–1452, 2011. 1
- [17] L. C. Evans. Partial differential equations and Monge-Kantorovich mass transfer. *Current developments in mathematics*, 1997(1):65–126, 1997. 3
- [18] J. H. Fitschen, F. Laus, and B. Schmitzer. Optimal transport for manifold-valued images. In *International Conference on Scale Space and Variational Methods in Computer Vision*, pages 460–472. Springer, 2017. 3
- [19] I. Goodfellow, J. Pouget-Abadie, M. Mirza, B. Xu, D. Warde-Farley, S. Ozair, A. Courville, and Y. Bengio. Generative adversarial nets. In *NIPS*, 2014. 1, 2
- [20] I. Gulrajani, F. Ahmed, M. Arjovsky, V. Dumoulin, and A. Courville. Improved training of Wasserstein GANs. *NIPS*, 2017. 1, 2, 4, 5, 6, 8
- [21] Z. Huang and L. Van Gool. A Riemannian network for SPD matrix learning. In *AAAI*, 2017. 3
- [22] Z. Huang, R. Wang, S. Shan, X. Li, and X. Chen. Log-Euclidean metric learning on symmetric positive definite manifold with application to image set classification. In *ICML*, 2015. 3, 4
- [23] A. Krizhevsky and G. Hinton. Learning multiple layers of features from tiny images. *Technical report, University of Toronto*, 2009. 4
- [24] F. Laus, M. Nikolova, J. Persch, and G. Steidl. A non-local denoising algorithm for manifold-valued images using second order statistics. *SIAM Journal on Imaging Sciences*, 10(1):416–448, 2017. 1

- [25] S.-M. Lee, A. L. Abbott, and P. A. Araman. Dimensionality reduction and clustering on statistical manifolds. In *CVPR*, 2007. 4
- [26] N. Lei, K. Su, L. Cui, S.-T. Yau, and D. X. Gu. A geometric view of optimal transportation and generative model. *arXiv preprint arXiv:1710.05488*, 2017. 3
- [27] G. Loeper. Regularity of optimal maps on the sphere: The quadratic cost and the reflector antenna. *Archive for rational mechanics and analysis*, 199(1):269–289, 2011. 3
- [28] X. Mao, Q. Li, H. Xie, R. Y. Lau, Z. Wang, and S. P. Smolley. Least squares generative adversarial networks. *ICCV*, 2017. 1, 2, 6
- [29] A. v. d. Oord, N. Kalchbrenner, and K. Kavukcuoglu. Pixel recurrent neural networks. *arXiv preprint arXiv:1601.06759*, 2016. 4
- [30] X. Pennec, P. Fillard, and N. Ayache. A Riemannian framework for tensor computing. *IJCV*, 66(1):41–66, 2006. 1, 3
- [31] A. Radford, L. Metz, and S. Chintala. Unsupervised representation learning with deep convolutional generative adversarial networks. *arXiv preprint arXiv:1511.06434*, 2015. 1, 2, 6
- [32] G. Steidl, S. Setzer, B. Popilka, and B. Burgeth. Restoration of matrix fields by second-order cone programming. *Computing*, 81(2):161–178, 2007. 1
- [33] C. Villani. *Optimal transport: old and new*, volume 338. Springer Science & Business Media, 2008. 3
- [34] J. Weickert, C. Feddern, M. Welk, B. Burgeth, and T. Brox. Pdes for tensor image processing. *Visualization and Processing of Tensor Fields*, pages 399–414, 2006. 1
- [35] M. Welk, C. Feddern, B. Burgeth, and J. Weickert. Median filtering of tensor-valued images. In *Joint Pattern Recognition Symposium*, pages 17–24. Springer, 2003. 1
- [36] J. Zhao, M. Mathieu, and Y. LeCun. Energy-based generative adversarial network. *arXiv preprint arXiv:1609.03126*, 2016. 1, 2